

Surface constrained electron-hole rich species active in the electrocatalytic water splitting

Juan Velasco-Vélez (✉ velasco@fhi-berlin.mpg.de)

Fritz-Haber-Institut der Max-Planck-Gesellschaft <https://orcid.org/0000-0002-6595-0168>

Emilia Carbonio

Helmholtz-Center Berlin for Materials and Energy

Cheng-Hao Chuang

Tamkang University

Cheng-Jhih Hsu

Tamkang University

Jyh-Fu Lee

National Synchrotron Radiation Research Center

Rosa Arrigo

University of Salford

Michael Hävecker

Max Planck Institute for Chemical Energy Conversion

Ruizhi Wang

University of Cambridge

Milivoj Plodinec

Fritz-Haber-Institut der Max-Planck-Gesellschaft

Alba Centeno

Graphenea

Amaia Zurutuza

Graphenea

Lorenz Falling

Fritz-Haber-Institut der Max-Planck-Gesellschaft

Rik Mom

Fritz-Haber-Institut der Max-Planck-Gesellschaft

Stephan Hofmann

University of Cambridge <https://orcid.org/0000-0001-6375-1459>

Robert Schlögl

Fritz Haber Institute of the Max Planck Society

Axel Knop-Gericke

Fritz-Haber-Institut der Max-Planck-Gesellschaft

Travis Jones (✉ trjones@fhi-berlin.mpg.de)

Article

Keywords: electronic structure, IrO_x centers, electrocatalytic oxidation of water, oxygen evolution reaction, surface to bulk ratio

Posted Date: December 15th, 2020

DOI: <https://doi.org/10.21203/rs.3.rs-118932/v1>

License:   This work is licensed under a Creative Commons Attribution 4.0 International License.
[Read Full License](#)

Abstract

Iridium and its oxides/hydroxides are the best candidates for the oxygen evolution reaction under harsh acidic conditions owing to the low overpotential and the high corrosion resistance observed for Ir-based anodes. Herein, by means of cutting edge *operando* surface and bulk sensitive X-ray spectroscopy techniques, specifically designed electrode nano-fabrication and *ab initio* DFT calculations, we were able to reveal the electronic structure of the active IrO_x centers (i.e. oxidation state) during electrocatalytic oxidation of water in the surface and bulk of high-performance Ir-based catalysts. We found the oxygen evolution reaction is controlled by the formation of empty Ir 5d states in the surface ascribed to the formation of formally Ir^V species leading to the appearance of electron-deficient oxygen species bound to single iridium atoms (μ_1 -O and μ_1 -OH) that are responsible for water activation and oxidation, due to the bound oxygen's transformation into an oxyl susceptible to nucleophilic attack water. Oxygen bound to three iridium centers (μ_3 -O) remains the dominant species in the bulk but do not participate directly in the electrocatalytic reaction, suggesting bulk oxidation is limited. In addition a high coverage of a μ_1 -OO (peroxo) species during the OER is excluded. Moreover, we provide the first photoelectron spectroscopic evidence in bulk electrolyte that the higher surface to bulk ratio in thinner electrodes enhances the material usage involving the precipitation of a significant part of the electrode surface and near-surface active species.

Main

Water splitting is among the most important electrochemical processes for the storage of renewable energy as the molecular hydrogen produced at the cathode can be used as a carbon-free energy vector¹⁻³. However, anode corrosion under acidic conditions and anodic polarization shortens material lifetimes leading to increased costs⁴⁻⁶. Among all the materials investigated for the oxygen evolution reaction (OER), only iridium and its oxides/hydroxides are known to combine low overpotential and corrosion resistance under harsh acidic conditions^{7,8}. Unfortunately, iridium is also one of the scarcest elements on earth, thus synthetic strategies for optimizing its usage are required⁹. To develop such strategies it is important to understand what drives stability and activity in these materials. The presence of a distribution of surface species with a mixed oxidation state between Ir^{III} and Ir^{VI} are suggested^{10,11} to be critical in the nature of the high activity¹² shown by this element. We reason that determining the electronic structure characteristics responsible for the peculiar reactivity of IrO_x for the OER, as well as quantifying the amount of the material and location of the active species participating in the reaction, is key to optimize its electrochemical performance and usage. Herein, we combine surface and bulk sensitive X-ray absorption spectroscopy (XAS) and X-ray photoelectron spectroscopy (XPS) together with the precise nano-fabrication of nanostructure electrodes and *ab initio* calculations to determine the nature of the active species and their distribution in the surface and near-surface region during the electro-catalytic oxidation of water.

Electrodes Fabrication And Characterization

Two different electrodes with different surface to bulk ratios were fabricated and compared, namely a 20 nm thin-film and 2.5 nm nanoparticles (NPs) on a graphene current collector electrodes. Fig. 1A shows a top view scanning electron microscopy (SEM) image of the sputtered thin-film electrode. The thin-film consists of interconnected polycrystalline islands with a thickness of 20 nm. In contrast, Fig. 1B shows the TEM image of isolated 2.5 nm IrO_x NPs supported on conductive bi-layer graphene. Owing to the structural differences, the thin-film can be considered a bulk model whereas the high surface to bulk ratio of the NPs makes them a surface model. Anodic oxidation of metallic iridium is reported to result in better performing catalysts than thermal activation, due to the existence of highly hydrated species forming an oxyhydroxide upon electro-oxidation¹³. Hence, the sputtered electrodes were oxidized/activated prior their use in OER by several potential scans between open circuit voltage (OCV) and 1.2 V at 20 mV/s scanning rate in a 50 mM H₂SO₄ electrolyte (potentials are not *iR* corrected). As expected, this procedure resulted in the development of an increasingly larger anodic peak in the cyclic voltammogram (CV), where the peak height increased with the number of cycles¹⁴. The condition of maximum peak height corresponds to the highest electrode activity for thin-films and NPs¹⁵. The TEM (Fig. 1B) images of the sputtered iridium particles on the free-standing bi-layer graphene show that they are homogeneously distributed after activation; the estimated coverage factor is around 20% of the surface and the average particle size is ~2.5 nm. Contact of the IrO_x NPs onto graphene is assured by a chemical bond between the surface Ir atoms and the oxygen species present at the edges and vacancies of graphene¹⁶. According to the SEM image in Fig. 1A, we estimate a surface area of about 1.5-2.0 monolayer (ML) for the thin-film and about 1/3 ML for the nanoparticles. The fast Fourier transform (FFT) proves the existence of reduced metallic iridium NPs. Such beam induced reduction is common in non-stoichiometric oxides. One additional ring can be ascribed to stoichiometric IrO₂.

The electrochemical performance of the Ir thin-film and Ir NP electrodes are compared in Fig. 1C and 1D. The CVs were acquired at room temperature (25°C), in de-aerated 0.1 M H₂SO₄ with N₂ continually bubbled in the electrolyte at a scan rate of 20 mV/s using Pt and Ag/AgCl (saturated in KCl) as counter and reference electrodes, respectively. The CVs show two broad oxidation waves, labeled I and II, and two broad reduction waves, labeled IV and V, due to formally Ir^{III}/Ir^{IV} and Ir^{IV}/Ir^V redox couples, respectively^{11,17,18}. An additional current (point III in Fig. 1C and 1D) is ascribed to the oxidation of water. The CVs in Fig. 1C and 1D indicate that both the thin-film and bi-layer graphene coated with Ir NPs behave similarly. Therefore, it is expected that similar active species are involved during the electrocatalytic oxidation of water to dioxygen on both the thin-film and iridium NP electrodes. It is generally accepted that these active sites are hydrated Ir-oxyhydroxides formed *in situ* during OER^{19,20}, where the Ir oxyhydroxide-based OER is stable for high-current water electrolysis under acidic conditions²¹.

Probing the bulk species formed during the water oxidation

In order to determine the nature of the active species, the electronic structure modification that the electrodes undergo during the electrocatalytic oxidation of water was investigated by means of *operando* XAS. The electrocatalysts were characterized first using XAS in total fluorescence yield (TFY) mode at the Ir L₃-edge using a homemade *in situ* electrochemical cell²², more details can be found in the supplementary information (SI). Using a 100 nm thick SiN_x membrane, which is transparent to the incoming and out-going photons, it is possible to investigate the variations in the electronic structure using photon-in/photon-out (PIPO) techniques in the hard X-ray regime. An advantage of this approach is that it enables the study of electrochemical reactions with aqueous electrolytes (i.e. 100 mM H₂SO₄). Fig. 2A and 2B show the detection scheme with the thin-film and free standing bi-layer graphene decorated with Ir NPs. For both materials it is possible to perform measurements in TFY-XAS by collecting the photons emitted during the fluorescence decay follow the absorption process; this signal comes from the surface and bulk of the materials. Therefore, TFY-XAS provide information associated with the whole electrode (bulk and surface) in the case of the Ir thin-film. However, in the case of the NPs, due to the average film thickness of ~6 monolayers (MLs), the surface signal is enhanced, despite the methodology not being a surface sensitive technique. Moreover, the free standing graphene allows the collection of photoelectrons (by a semispherical electron analyser) from the side exposed to the electrolyte, thereby enabling the acquisition of photoelectron spectra (PES)^{23,24}. Meanwhile, the thin-film electrode (20 nm) only yields photoelectrons from the side where the electrode is exposed to the incident X-ray photons, as shown in Fig. 2A, making it impossible to investigate the electrified solid-liquid interface of such a thick working electrode using soft PES. Note that PES is a surface sensitive technique due to the short inelastic mean free path (IMFP) of photoelectrons in solids or liquids^{25,26}, making it an excellent complement to TFY-XAS.

Fig. 2C shows the Ir L₃-edge spectra collected under *operando* conditions. The Ir L₃-edge probes the dipole allowed transitions from a core Ir 2p_{3/2} electron to the partially occupied Ir 5d and Ir 6sp orbitals, which are hybridized with the O 2p orbitals²⁷. Transitions to the 5d orbitals are lower in energy and well separated from transitions to the 6sp. These 2p to 5d transitions give rise to the so-called white-line. While the large lifetime broadening (about 5 eV, see SI) does not allow the discrimination of fine structure in the white-line due to, for instance, transitions into t_{2g}-like and e_g-like 5d orbitals, analysis of the white-line intensity can still give insight into the electronic structure of iridium. In particular, a sum-rule relates the total number of 5d holes to the integral area of the white-line^{11,27}; that is, the white-line is linearly proportional to the iridium oxidation state²⁸. Note that while the sum-rule is a property of the dipole operator and rigorously holds^{29,30} for L₃ + L₂, previous work shows no change in the L₃:L₂ branching ratio for oxidized iridium compounds, making L₃ alone sufficient for a white-line analysis²⁸. The ability of the bulk sensitive TFY-XAS measurements to reveal changes in average Ir oxidation states is apparent from Fig. 2C. Using the maximum intensity of the Ir L₃ edge as a measure of average Ir oxidation state an increase in the number of Ir 5d holes can be seen in both the thin-film and NP samples under anodic polarization. This increase in average oxidation state is reversed under open circuit voltage (OCV). Similar trends were reported previously by *in situ* characterization of iridate working electrodes³¹⁻³⁴. Before

turning to a quantitative evaluation of this behavior, however, the details of the proportionality between white-line intensity and Ir oxidation state must be found. To establish a connection between the white-line intensity and the number of 5d holes on Ir we analyzed a series of reference samples, including: Ir⁰, IrCl₃, IrO₂, and IrO_x (reference samples details can be found in the SI)³⁴. An iridium foil was used for Ir⁰. IrCl₃ powder was used as an Ir^{III} reference, and IrO₂ rutile-type powder was taken as a Ir^{IV} reference. In addition, an amorphous IrO_x catalyst rich in active species¹⁷ was used to compare with the catalysts used in this work. Note that the Ir⁰ (foil) white-line can be artificially enhanced due to the existence of a native oxide layer and the fact that this spectrum is collected in TFY mode, self-absorption effects are also possible. However, the oxide layer is not a problem since it is thin compare to the bulk with minor contribution to the white-line intensity.

Fig. 3A1 shows the Ir L₃ spectra of the reference samples including the background subtraction and remaining signal, which relates the number of Ir 5d holes to the integral area of the white-line²⁸. These measurements clearly show an increase in the Ir L₃-edge white-line intensity for the different samples following the trend: Ir⁰<IrCl₃<IrO₂<IrO_x. Moreover, in Fig. 3A2 the maximum intensity of the white-line is linearly correlated with the integral intensity and, therefore, Ir oxidation state. Thus, for simplicity we employ the maximum white-line intensity as a measure of the Ir oxidation state. Similarly, the Ir L₃-edges computed using the Bethe-Salpeter equation show the same trend continues through the bulk oxides Ir₂O₅ and IrO₃ (Fig. 3B), see SI for more details (Fig. S3). From the white-line integration of the experimental data, Fig. 3A2 shows the percent increase in the Ir 5d density of electron-holes referred to IrCl₃ and the equivalent oxidation state. Therefore, an oxidation state of +4 correspond to an increase of ~22% of the white-line intensity with respect to +3 (IrCl₃ sample), and a change of ~32% for the case of IrO_x corresponding to a +4.7 average oxidation state. This increase is supported by its comparison with Ir⁰, where an increase of a 52% of the white-line intensity is found for +4 and 65% for IrO_x, corresponding to a +4.6 average oxidation state. Performing a similar quantification using the simulated data shows the maximum white-line intensity changes linearly with the Löwdin charge on Ir in the bulk phases as well as across various surface Ir species bound to O, OH, OOH, and OO on IrO₂ surfaces spanning formal oxidation states from <IV to >VII (see SI for details, Fig. S4 and S5), suggesting no significant changes in intensity variation should be expected at higher oxidation states for the iridium oxyhydroxides. One can also consider that the change in the oxidation can often be correlated to the shift in the peak position, using this approach an average experimental oxidation state of +4.3 is found for IrO_x, similar to the integration of the white-line Fig. 3A2. Both approaches yield an average oxidation state for IrO_x under vacuum >IV suggesting the presence of Ir^V, in agreement with the Ir^V reported to appear in IrO_x during reaction conditions using a similar analysis, but significantly less than the Ir^{VI} reported¹¹ to appear in Ni-leached IrNiO_x. To see if evidence for such high oxidation state Ir emerge for Ir NPs and thin-films under reaction conditions we return to *in situ* measurements.

Fig. 4 shows how the measured white-line intensities change with applied bias. The spectra were collected under chronoamperometric (CA) control, and ~1 hour was required to record each Ir L₃-edge spectrum. This fact, together with the constant current observed under the applied potential, verifies that the spectra were collected under steady state conditions, which is important to assure their fidelity. The white-line intensity, and hence Ir oxidation state, can be seen to remain constant up to 0.7 V, above which the materials are oxidized. From the Ir Pourbaix diagram, Ir⁰ is expected below 0.73 V,³⁵ making it tempting to assign the starting state of the film and NPs to Ir⁰. However, the surfaces likely remain partially oxidized after the CV activation steps³⁶ making an assignment to Ir^{III} more appropriate, as a consequence of surface irreversible oxidation state, as confirmed by XPS below. At 1.0 V Ir^{IV} has become the stable phase on the Pourbaix diagram, which is further supported by the CVs of the film and NPs showing 1.0 V is above the Ir^{III}/Ir^{IV} redox couple, but below the transition assigned to Ir^{IV}/Ir^V. At 1.0 V the near-surface region is then expected to be Ir^{IV}. The higher white-line intensities confirm oxidation, with the ~30% increase for the Ir NPs in line with an increase to +4.5, assuming Ir^{III} to start. The higher white-line intensity of the NPs compared to the thin-films is likely due to incomplete oxidation of the bulk of the 20 nm thin-films^{18, 37, 38}. At 1.6 V, though no further increase in white-line intensity is observed for the thin-films, whereas the NPs show an additional ~4% increase above that observed at 1.0 V suggesting the co-existence of Ir^{IV}/Ir^V, or higher oxidation states, on the catalyst surface. To gain a better understanding of what these species may be, we turned to *ab initio* calculations.

In order to provide a better description of the observed changes in the white-line spectra, these reference and *operando* measurements were compared with the DFT calculated Ir L₃-edge spectrum (details can be found in the SI). We begin with the lowest energy, in vacuum, IrO₂ surface, (110), as a model for the DFT calculations³⁹. The surface was first fully hydrogenated as shown in Fig. 5. It was then successively oxidized by following a series of proton coupled electron transfers to explore the adsorbates argued to be present under OER conditions³⁹, see Fig. 5. The Ir L₃-edge white-line intensities of these surfaces were computed and plotted against the number of electrons transferred from the hydrogenated surface unit cell to reach the desired surface oxidation state. From Fig. 5 it can be seen that only the surface Ir atoms respond to the oxidation, with the first subsurface layer already converged to the L₃-edge white-line intensity of bulk Ir^{IV}. The average surface oxidation state can be seen to increase from a white-line intensity below Ir^{IV} when μ_1 -H₂O and μ_2 -OH are present—where the subindex indicates the number of iridium atoms bound to an oxygen atom—to a value consistent with bulk Ir^V when μ_1 -O and μ_2 -O are present. The former is close to the +3.5 average formal oxidation state for the surface Ir atoms found by simple bond counting.

Removing H⁺ and e⁻ from μ_1 -H₂O on the (110) surface yields a surface with μ_1 -OH and μ_2 -OH that is predicted to be stable up to 0.7 V.³⁹ The average formal surface oxidation state of Ir on this surface is +IV, in-line with the computed L₃-edge white-line intensity, Fig. 5. At 0.7 V the surface termination is predicted to transform into μ_1 -OH and μ_2 -O, with an average Ir surface oxidation state of +4.5, in general agreement

with the experimental results on the NPs. Above 1.2 V both a surface μ_1 -O or μ_1 -OO have been predicted to be stable^{17,39}. Of these, the μ_1 -O appears more likely on the NP surface owing to the small increase in white-line intensity observed experimentally between 1.0 V to 1.6 V, which is consistent with the increase in iridium formal oxidation state and the computed white-line intensity for transitioning from μ_1 -OH to μ_1 -O. The μ_1 -OO (and μ_1 -OOH) both show reduced white-line intensities relative to μ_1 -OH and μ_1 -O, and while we observed no evidence for such a reduction in intensity, it has been previously observed on IrO_x NPs at high applied potential⁴⁰.

We also considered the possibility that the NPs facet during anodic polarization, as above 1.1 V the (111) surface is thermodynamically favored³⁹. Following the same methodology as above, Fig. 5 shows the Ir L₃-edge white-line intensities as a function of the number of electrons transferred starting from a fully hydroxylated (111) surface, see SI for structures (Fig. S4). Here, though more points are included owing to the presence of four μ_2 -OH species in the unit cell, a similar trend emerges as found for the (110) surface, with the Ir L₃-edge white-line intensities reaching higher values due to the increased formal surface iridium oxidation states on the (111) vs. (110) surface. In particular, the Ir bound to μ_1 -O reaches a formal oxidation state exceeding Ir^{VI}. Such a species is predicted to appear once the bias reaches 1.1 V; above 1.2 V μ_1 -O may transform into a μ_1 -OO.³⁹ While we see no drop in white-line intensity on the NPs supporting the formation of μ_1 -OO, we cannot completely rule out the appearance of Ir^{VI} from XAS alone. Thus, we turned to XPS.

Probing The Surface Species Formed During The Water Oxidation

As a surface sensitive technique, XPS compliments the bulk sensitive XAS and offers the opportunity to gain deeper knowledge about the mechanism mediating the electrochemical oxidation of water on iridium oxide. The electronic structure of the IrO_x NPs on graphene was investigated at the Ir 4f core level using the facilities and *in situ* electrochemical flow cells described in the SI²⁴. The Ir 4f spectra depending on the applied potential are shown in Fig. 6A, as well as its comparison with the reference samples (bottom spectra) and the computed line shapes for the relevant species inferred through the XAS analysis (see Fig. S6 and S7). Computed XPS binding energies are summarized in Table S1.

At, and below, 0.7 V the NPs are composed of predominantly bulk Ir^{III}, with an Ir 4f binding energy of 62.3 eV.⁴¹ Once the electrode is polarized to 1.0 V, we know from XAS that the NPs are oxidized to Ir^{IV}, and possibly higher. From the simulations we find that Ir atoms on the surface of IrO₂ show normal Ir 4f binding energy shifts up to formal Ir oxidation states of, at least, 7.3, see Table S1, with the average formally Ir^V and Ir^{VI} species appearing near ~62.2 eV and ~62.7 eV, respectively. Thus, the Ir 4f shift is a good measure of iridium oxidation state for Ir atoms in a conductive matrix. However, this conductive matrix also influences the Ir 4f lineshape, making accurate speciation challenging. The computed Ir 4f spectra all show complex lineshapes due to conduction band screening, see Fig. 6B for computed XPS, similar to that observed in rutile-type IrO₂,^{10,42} where shake-up satellites are required to fit the spectral

envelope. The lineshape varies systematically with the formal oxidation state of Ir, with the primary satellite shifting closer to the main line with increasing iridium oxidation state, see Fig. 6B. Noting this behavior allows a suitable fit model to be developed.

Using this fit model we see that at an applied bias of 1.0 V, peaks appear at 61.8 eV and 62.5 eV, both of which show strong conduction band screening. The first of these peaks is consistent with the Ir^{4.3} bound to μ_1 -OH on the (110) surface. The species at 62.5 eV is consistent with the Ir^{5.3} bound to μ_1 -O on the (110) surface or the Ir^{5.7} bound to μ_1 -OH (or μ_1 -OOH) on the (111) surface. Thus, at 1.0 V the near surface region appears to be dominated by Ir^{IV}/Ir^V and μ_1 -OH/ μ_1 -O. These findings are in general agreement with predictions based on *ab initio* atomistic thermodynamics³⁹. Details of the parameters used for fitting the spectra can be found in the SI (Table S2), where a Shirley background is used.

Under OER conditions the species at 62.5 eV becomes the dominant species and no higher binding energy component is found. This suggests surface oxidation has occurred when increasing the bias from 1.0 V to 1.6 V, as shown in Fig. 6A, in agreement with the XAS -TFY *operando* measurements. With XPS, however, we can rule out the possibility of Ir oxidation states of Ir^{VI} and above since these would appear at higher binding energies than those observed. Thus, taking XPS and XAS together we tentatively assign the species appearing at 62.5 eV to a formally Ir^V species bound to μ_1 -O on the (110) surface. While small amounts of the Ir at this high binding energy has also been observed in both *ex situ*⁴³ and *in situ*⁴⁴ studies, the surface model system employed in this work allows us to show the formally Ir^V species is the dominant surface species under the OER, a key aspect in materials with a high surface to bulk ratio⁴⁵. When combined with *ab initio* simulation, this allows a more definitive assignment to be made. Moreover, from the simulations we see that at such high formal Ir oxidation states, the μ_1 -O species bound to Ir^V may also be referred to as O[•] owing to the strong radical character. This electron deficiency on μ_1 -O makes the oxygen susceptible to nucleophilic attack^{11,17,42,46}, suggesting the high activity of the Ir NPs is linked to electron hole-enrichment on μ_1 -O.

When the XPS and XAS measurements are compared another important aspect of the active state of the material can be seen, the relative thickness of the electron hole-enrichment beyond Ir^V is confined to the near surface region, while Ir^V may extend through the bulk. XPS shows surface and near-surface of the NPs are dominated by the formation of active Ir^{V+} (or O[•]) species that are active in the electrocatalytic oxidation of water. These active species contribute *ca.* ~4% to the overall Ir L₃ white-line intensity observed for the NPs when increasing the bias from 1.0 V to 1.6 V, while the Ir^{IV} bound to μ_3 -O species located in the bulk dominate the ~30% increase in white-line intensity seen when increasing the bias from 0.6 V to 1.0 V. By contrast, for the 20 nm films, surface oxidation past Ir^{IV} cannot be discerned from the bulk oxidation to Ir^{IV} owing to the overwhelming bulk signal.

Conclusions

In summary, the combination of *ab initio* calculations, XA and PE spectroscopies and nano-fabrication of thin-film IrO_x and free standing graphene decorated IrO_x NP electrodes provided relevant information related to the active sites of iridium-based electrocatalysts in the kinetically sluggish OER. It was found that the electrocatalytic activity of IrO_x is ascribed to the formation of formally Ir^V species bound to μ₁-O, where, due to the electron deficiency of these Ir sites the μ₁-O on the surface of the electrocatalyst transforms into an oxyl that is susceptible to nucleophilic attack by water. Our results show that the potential-dependent oxidation state changes in the IrO_x extend through the bulk for oxidation states below Ir^V but are constrained to the near-surface region for higher oxidation states, suggesting bulk oxidation is limited. Thus, the higher surface to bulk ratio of nano-structured materials enhances iridium usage and the participation of a significant larger amount of surface and near-surface active μ₁-O oxyls. In addition we provide evidence using bulk electrolyte for these changes using surface sensitive XPS, which is in good agreement with the bulk sensitive XAS-TFY measurements yielding a direct link between surface and bulk effects in electrocatalytic OER.

Methods

Electrode preparation

Graphene was grown by chemical vapor deposition (CVD) on a 20 μm thick Cu foil (Alfa Aesar 99.8%) as catalysts and CH₄ (diluted in Ar and H₂) at 1000 °C using an Aixtron BM Pro (4 inch) reactor yielding a continuous polycrystalline film with grain size in the range of ~20 μm, which was confirmed by scanning electron microscopy. The graphene layer was fixed to 500 nm of Poly(methyl methacrylate) PMMA (4 wt.% in anisole, 950k molecular weight) deposited by spin coating. After that, the copper support was eliminated by floating on a 50 mM aqueous solution of (NH₄)₂S₂O₈. The graphene/PMMA layer was floated in deionized water (DI-water) and transferred onto another graphene/copper foil and dried at 50 °C for 5 minutes. The resulting sample was floated again in the (NH₄)₂S₂O₈ solution to remove the copper foil before rinsing in DI-water. The PMMA/BLG layer was transferred to a Norcada[®] Si₃N₄ TEM grid with 500 nm diameter holes or onto a SiN_x membrane 100 nm thick for the TFY measurements^{47,48}. Finally, the PMMA was eliminated with acetone and the adherence between the BLG and the substrate is due to Van der Waals interaction ensuring stability for the electrodes. It produces a continuous film that can be used as an electrode in aqueous environments as electrocatalytic applications among others^{49,50}.

Fig. S1 A and B show the SEM measurements of the free standing graphene on the Si₃N₄ grid. The influence of holes is suppressed by the addition of a second graphene layer. Raman spectroscopy was used to check the lattice vibrations of the crystallized BLG which is sensitive in order to determine the graphitic character of this sample. Fig. S1 C shows the Raman spectra of different reference samples such as HOPG, single layer graphene (G), graphene oxide (GO), reduced graphene oxide (RGO), and the transferred BLG used in this study. The origin of the graphitic Raman spectrum is well established and is accepted that it presents three first order bands between 1000 cm⁻¹ and 3000 cm⁻¹: D band at ~1350

cm^{-1} , G band at $\sim 1580 \text{ cm}^{-1}$ with a shoulder at $\sim 1620 \text{ cm}^{-1}$.^{51,52} The D band is associated with defects that perturb the breathing modes of carbon rings. The G band is due to the in-plane phonons at the Brillouin zone centre. The 2D band is due to excitation of two phonons with opposite momentum in the highest optical branch near the K point and is sensitive to the number of graphene layers⁵³. The Raman spectrum of HOPG does not show a D band, which attributed to the small number of points defects, and attenuated 2D due to the excitation of two phonons with opposite momentum in the underlying layers. On the other hand, the graphene reference spectrum does not show a D band and the ratio of the 2D and G peak intensities, i.e., I_{2D}/I_G is approximately ~ 2 indicating a good graphitization and likely the absence of more underlying layers⁵⁴. Graphene oxide (GO) shows a I_{2D}/I_G ratio decreases and the D peak intensity increases, indicating an increase in the defect concentration. This trend in the peak intensity is not due to the presence of oxygen, as the similar behavior of the reduced graphene oxide (RGO) spectrum proves, indicating that the origin of this behavior is the existence of defects in the graphene lattice. The absence of the D band confirms the BLG is of high-quality with a low density of defects in the graphene lattice. In addition, the reduction in the I_{2D}/I_G ratio to approximately ~ 1.7 suggests the presence of an underlying graphene layer due to the excitation of phonons with opposite momentum, which reduces the intensity of the 2D.

The electrodes were deposited by sputtering using Cressington 208HR sputter coated machine loaded with an Ir target (99.99% from Elektronen-Optik-Service GmbH, Germany) in a 0.1 mbar Ar atmosphere at a current of 40 mA. The sputter time determined the thickness of the electrode: the nanoparticles were deposited for 5 s yielding the formation of a homogenous well distributed Ir NPs in the whole surface with NPs size ranging from 2 to 5 nm in the form of metallic iridium (Ir^0). The 20 nm thin-film electrodes were fabricated by sputtering onto a SiN_x membrane (100 nm thick and 5 mm x 5 mm, with a Si frame of 1 cm x 1 cm and 200 μm thick sourced from Norcada) in a 0.1 mbar Ar atmosphere at a current of 40 mA for 160 s. There are stoichiometric iridium oxide NPs that remain unaltered under the electron beam, being more stable than the non-stoichiometric iridium oxide (Ir_xO_y) nanoparticles. These particles are in the form of IrO_2 rutile with orientation (210) and 0.20 nm lattice constant and IrO_2 (201) and lattice plane distance of 0.26 nm both with tetragonal crystal structure, as shown in Fig. 1B. At higher magnification it was found that some of the iridium NPs are reduced to Ir^0 under vacuum conditions and in presence of the electron beam. It is a well know problem and is related to the existence of a non-stoichiometric iridium oxide (Ir_xO_y) giving Ir^0 (111) cubic structure with a lattice plane distance of 0.23 nm as a product of the reduction by the beam.

The electrodes were oxidized/activated for their use in OER by potential cycling by continuous cyclic-voltammogram (CV) between 0 V and 1.2 V vs. Ag/AgCl (DRIFREF-2SH, World Precision Instruments, US) and Pt counter electrode for 10 minutes in 0.1 M of H_2SO_4 (EMSURE 97%, Merck, Germany) in Mili-Q water (18.2 M Ω) at a rate of 20 mV/s at room temperature (RT), 25°C. The continuous cycling between open circuit voltage (OCV) and OER in a H_2SO_4 electrolyte at RT results in the electrode activation.

In situ electrochemical cell

The EC-cell used for hard X-ray measurements is shown in Fig. S2A, where the flow of liquid was assured with a peristaltic micro pump. This cell is based on a 100 nm thick SiN_x membrane, transparent to the incoming X-ray photons, possible photon-in/photon-out (PIPO) techniques possible in the hard X-ray regimen, thereby enabling the study of electrochemical reactions with aqueous electrolyte. The SiN_x window is 100 nm thick, with an area of 5 mm x 5mm and silicon frame of 1 cm x 1 cm and 200 μm thick²².

For the *in situ* XPS characterization, the liquid flow cell^{55,56} was operated inside the main chamber of the AP-XPS endstation of the ISSS of the synchrotron facility BESSY II (Berlin, Germany) under a main chamber of ~10⁻⁷ mbar background pressure while aqueous electrolyte (0.1 M H₂SO₄) is flowed (1 ml/min) on the back side of the free standing graphene membrane described above, which is used as the working electrode. The continuous flow of liquid was assured by a syringe pump, 260D Teledyne Isco (Lincoln, USA). The main body of the electrochemical cell is made of polyether ether ketone (PEEK), which is an exceptional electrical insulator and chemically inert. The sealing was assured with several Kalrez O-rings, which have good chemical stability. The cell contains two additional electrodes, the counter-(platinum) and reference-electrode (Ag/AgCl DRIFEF-2SH, World Precision Instruments, USA). A cross-section of the cell is depicted in Fig. S2B. The Ir 4f spectra were collected with a kinetic energy of the photoelectrons of 600 eV at different potentials. At open circuit potential (OCP) the Ir 4f peak consists of two main peaks ascribed to the spin orbit split Ir 4f7/2 and Ir 4f5/2 states.

Beamlines

In situ synchrotron radiation based experiments were performed at the ISSS beamline of BESSY II in Berlin (Germany). In this facility, the photons are sourced from a bending magnet (D41) and a plane grating monochromator (PGM) yielding an energy range from 80 eV to 2000 eV (soft X-ray range), a flux of 6x10¹⁰ photons/s with 0.1 A ring current using a 111 μm slit and a 80 μm x 200 μm beamspot size. The *operando* measurements were accomplished in the ambient pressure X-ray photoelectron spectrometer (AP-XPS) end-station of the ISSS beamline, which is equipped with a SPECS PHOIBOS 150 NAP hemispherical analyzer.

Hard X-ray absorption measurements at the Ir L₃-edge were performed at the beamline BL17C1 of the National Synchrotron Radiation Research Center (NSRRC) in Hsinchu (Taiwan). The photons are sourced from a 25 poles wiggler (W20) with 20 cm period length and a focus spot size of 2 mm x 6 mm. The excitation energy ranges from 4.8 keV up to 14.2 keV. The signal was collected in transmission mode for the powder samples and in total fluorescence yield (TFY) mode for the foil and *in situ* EC-cell experiments, using an ionization chamber detector.

Electrolyte preparation

The electrolyte was prepared by diluting 9.8 g of H₂SO₄ (purity 98%, Alfa Aesar, Massachusetts, USA) in 1 L of Milli-Q water (18.2 MΩ) at room temperature (RT), 25 °C. The electrolyte was continuously saturated

by bubbling pure N₂ gas, which minimizes the presence of other dissolved gases in the electrolyte. The electrolyte is acidic with pH~1.

Potentiostat

Potentiometric control was assured with a Biologic SP-300 (Seyssinet-Pariset, France) allowing different potentiometric and amperometric controls. The experiments were performed in the presence of aqueous electrolyte where the measurements were acquired using the electrochemically activated IrO_x electrode in presence of 100 mM H₂SO₄ aqueous electrolyte (pH~1) saturated in N₂ (gas) at the same time that the electrolyte was continuously refreshed by a peristaltic pump (Pt counter electrode and Ag/AgCl reference), which minimizes the possibility to form trapped gas bubbles that can potentially influence the electrochemical cell performance.

Reference samples

Commercially available iridium powders were purchased from Sigma-Aldrich (99.9% trace metals basis) and AlfaAesar (Premion, 99.99% trace metals basis). In addition, Ir foil was purchased from Mateck (99.99% metals basis). The AlfaAesar powder was used as received and the SigmaAldrich powder was washed in Milli-Q water and calcined at 800 °C in O₂ for 50 hours. The AlfaAesar powder is X-ray amorphous (IrO_x) while the calcined sample of SigmaAldrich exhibits the rutile-type structure (IrO₂). More details of the sample preparation/characterization can be found elsewhere¹⁰. The Ir foil was subjected to several cycles of sputtering in Ar⁺ atmosphere and annealing in H₂ atmosphere and shows a purely metallic phase.

Calculations

Density functional theory calculations were performed at the PBE level using the Quantum ESPRESSO package⁵⁷ using pseudopotentials from the PSLibrary⁵⁸ with a kinetic energy (charge density) cutoff of 60 Ry (600 Ry). For bulk rutile-type IrO₂ calculations a (12 × 12 × 12) *k*-point mesh was used with Marzari-Vanderbilt cold smearing using a 0.01 Ry smearing parameter⁵⁹. The structure for bulk Ir₂O₅ was found using USPEX⁶⁰ with Quantum ESPRESSO. A starting population of 28 individuals was employed with a fixed composition of Ir₂O₅. The search was allowed to run until the lowest energy structure remained unchanged for 5 generations. The resulting low energy *C2/m* structure from this search was further optimized with Quantum ESPRESSO using a (6 × 6 × 6) *k*-point mesh and is shown in Fig. S3A. The structure for bulk IrO₃ was taken from the Materials Project (ID:mp-1097041).⁶¹ The orthorhombic *Cmcm* structure was further optimized Quantum ESPRESSO using a (6 × 6 × 6) *k*-point mesh and is shown in Fig. S3B. Rutile-type (110) surfaces were modeled with symmetric 5-layer slabs separated by 20 Å of vacuum using a (6 × 12 × 1) *k*-point mesh and 0.01 Ry cold smearing. Rutile-type (111) surfaces were modeled with 11-layer slabs separated by 20 Å of vacuum using a (4 × 4 × 1) *k*-point mesh and 0.01 Ry cold smearing. Surface calculations included spin-polarization. A 7-layer rutile-type IrO₂ (001) surface

was also included to access higher Ir surface oxidation states and was computed using a $(6 \times 6 \times 1)$ k -point mesh and 0.01 Ry cold smearing with 20 Å of vacuum separating periodic images.

XAS spectra were computed with a resolvent-based Bethe-Salpeter Equation (BSE) approach⁶² using the wavefunctions from Quantum ESPRESSO with the core-level BSE solver in the OCEAN package⁶³. For these calculations normconserving pseudopotentials were used with a kinetic energy cutoff of 120 Ry. Empty bands were included to up to 200 eV above the Fermi energy (E_F). Other parameters matched the total energy calculations. All XAS spectra were broadened with a 5.2 eV wide Lorentzian to capture the lifetime broadening at the Ir L_3 edge⁶⁴. Spectra were aligned using Δ SCF calculations⁶⁵. The excited state of each absorbing atom was computed separately using a 2p core-hole on the absorbing atom, and the excited electron was included in the simulation. For bulk IrO₂ Δ SCF calculations were performed using a $(4 \times 4 \times 4)$ supercell, while for the (110) and (111) surfaces (3×6) and (3×3) supercells were used, respectively. The spectra were aligned to experiment using bulk rutile-type IrO₂.

XPS spectra were computed using a Hopfield perturbation model⁶⁶. Following reference⁶⁷, the initial density of states (DOS) of the photoexcited atom were taken from the project Ir 5d DOS of the ground state, and the final density of states were taken from the project Ir 5d DOS of the atom with an Ir 4f corehole using the same supercells as the Δ SCF calculations used for XAS alignment. Constant Gaussian broadening (0.3 eV) was included along with energy dependent Lorentzian broadening. Lorentzian broadening used an empirical Seah-Dench like model⁶⁸, where the energy dependent line width above E_F is given by: $\Gamma(E) = \Gamma_0 + \Gamma_{\max}[1/2 + 1/\pi \arctan(e^{-1/e^2})]$ with $e = (E - E_F)/(E_C - E_F)$. The parameters Γ_{\max} and E_C were taken as 22 and 8 eV, respectively, while Γ_0 was taken as the tabulated natural line width, 0.3 eV.⁶⁹ The N₆ and N₇ edges were broadened separately and the spin-orbit splitting was taken from the free atom value. The Ir 4f shifts were computed by way of Δ SCF calculations using the total energy differences from the ground state and excited calculations. The spectra were aligned to experiment using bulk rutile-type IrO₂.

Declarations

Acknowledgements

The authors acknowledge BESSY II/ HZB for allocating beamtime within the project number 16103418CR. This work was supported by the Ministry of Education and Science of the Russian Federation (RFMEFI61614 × 0007) and the Bundesministerium für Bildung und Forschung (BMBF-05K14EWA) through the joint Russian-German research project “SYnchrotron and NEutron STudies for Energy Storage (SYNESTESia).” We thank DAAD for financial support in the framework of Taiwanese-German collaboration (projects ID 57218279 and 57392335). C.H.C. acknowledges financial support from projects 104-2112-M-032-005-MY2 and 105-2911-I-032-501. S.H. acknowledges funding from EPSRC (EP/K016636/1) and R.W. acknowledges EPSRC Doctoral Training Award (EP/M506485/1). We

thank the High-Performance Computing Center Stuttgart (HLRS) for access to the Hawk supercomputer as part of the ECHO project.

References

1. Schlögl, R. The role of chemistry in the energy challenge. *ChemSusChem* **3**, 209–222 (2010).
2. Turner, J. A. Sustainable hydrogen production. *Science* **305**, 972–974 (2004).
3. Chu, S. et al. Opportunities and challenges for a sustainable energy future. *Nature* **488**, 294–303 (2012).
4. Walter, M. G. et al. Solar water splitting cells. *Chem. Rev.* **110**, 6446–6473 (2010).
5. Gong, K. et al. Nitrogen-doped carbon nanotube arrays with high electrocatalytic activity for oxygen reduction. *Science* **323**, 760–764 (2009).
6. Gorlin, Y. et al. A bifunctional nonprecious metal catalyst for oxygen reduction and water oxidation. *JACS* **132**, 13612 (2010).
7. Lee, Y. et al., Synthesis and activities of rutile IrO₂ and RuO₂ nanoparticles for oxygen evolution in acid and alkaline solutions. *J. Phys. Chem. Lett.* **3**, 399–404 (2012).
8. Wen, T. C. et al. Hydrogen and oxygen evolutions on Ru-Ir binary oxides., *J. Electrochem. Soc.* **139**, 2158–2163 (1992).
9. Reier, T. et al. Electrocatalytic oxygen evolution reaction (OER) on Ru, Ir, and Pt catalysts: a comparative study of nanoparticles and bulk materials. *ACS Catalysis* **2**, 1765–1772 (2012).
10. Pfeifer, V. et al. The electronic structure of iridium and its oxides. *Sur. Intef. Anal* **48**, 261–273 (2016).
11. Nong, H. N. et al. A unique oxygen ligand environment facilitates water oxidation in hole-doped IrNiO_x core-shell electrocatalysts. *Nat. Cat.* **1**, 841 (2018).
12. Kasian, O. et al. The common intermediates oxygen evolution dissolution reactions during water electrolysis on iridium. *Ang. Chem. Int. Ed.* **57**, 2488–2491 (2018).
13. Ouattara, L. et al. Electrochemical comparison of IrO₂ prepared by anodic oxidation of pure iridium and IrO₂ prepared by thermal decomposition of H₂IrCl₆ precursor solution. *J. Appl. Electrochem.* **39**, 1361–1367 (2009).
14. Gottesfeld, S. et al. Electrochemical and optical studies of thick oxide layers on iridium and their electrocatalytic activities for the oxygen evolution reaction. *J. Electroanal. Chem. Interf. Electrochem.* **86**, 89–104 (1978).
15. Song, S. et al., Electrochemical investigation of electrocatalysts for the oxygen evolution reaction in PEM water electrolyzers. *Int. J. Hyd. Ener.* **33**, 4955–4961 (2008).
16. Rojas, J. V. et al. Single step radiolytic synthesis of iridium nanoparticles onto graphene oxide. *App. Surf. Sci.* **357**, 2087–2093 (2015).
17. Frevel, L. J. et al. In Situ X-ray Spectroscopy on the Electrochemical Development of Iridium Nanoparticles in Confined Electrolyte. *J. of Phys. Chem. C* **124**, 14941–14943 (2019).

18. Pfeifer, V. et al. In situ observation of reactive oxygen species forming on oxygen-evolving iridium surfaces. *Chem. Sci.* **8**, 2143–2149 (2017).
19. Frazer, E. J. et al. The oxygen evolution reaction on cycled iridium electrodes. *J. Elec. Chem. Interf. Electrochem.* **102**, 127–130 (1979).
20. Willinger, E. et al. Identifying key structural features of IrO_x water splitting catalysts. *JACS* **139**, 12093–12101 (2017).
21. Massué, C. et al. High-performance supported iridium oxohydroxide water oxidation electrocatalysts. *ChemSusChem* **10**, 1943–1957 (2017).
22. Velasco-Vélez, J. J. et al. The role of the copper oxidation state in the electrocatalytic reduction of CO₂ into valuable hydrocarbons. *ACS Sus. Chem. & Eng.*, **7**, 1485–1492 (2018).
23. Kolmakov, A. et al. Graphene oxide windows for in situ environmental cell photoelectron spectroscopy. *Nat. Nanotech.* **6**, 651–657 (2011).
24. Velasco-Vélez, J. J. et al. Photoelectron Spectroscopy at the Graphene–Liquid Interface Reveals the Electronic Structure of an Electrodeposited Cobalt/Graphene Electrocatalyst. *Ang. Chem. Int. Ed.* **54**, 14554–14558 (2015).
25. Velasco-Vélez, J. J. et al. The structure of interfacial water on gold electrodes studied by x-ray absorption spectroscopy. *Science* **346**, 831–834 (2014).
26. Itkis, D. M. et al. Probing operating electrochemical interfaces by photons and neutrons. *ChemElectroChem* **2**, 1427–1445 (2015).
27. Velasco-Vélez, J. J. et al. Electrochemically active Ir NPs on graphene for OER in acidic aqueous electrolyte investigated by in situ and ex situ spectroscopies. *Surf. Sci.* **681**, 1–8 (2019).
28. Clancy, J. P. et al. Spin-orbit coupling in iridium-based 5 d compounds probed by x-ray absorption spectroscopy. *Phys. Rev. B*, *86*(19), 195131 (2012).
29. Jo, T. X-ray magnetic circular dichroism, symmetry and orbital magnetization. *J. Phys. Soc. Japan* **62**, 1814–1815 (1993).
30. Dehmer, J. L. et al. Potential-Barrier Effects in Photoabsorption. III. Application to 4 d-Shell Photoabsorption in Lanthanum. *Phys. Rev. B* **5**, 1792–1796 (1972).
31. Hüppauff, M. et al. Valency and structure of iridium in anodic iridium oxide films. *J. Electrochem. Soc.* **140**, 598–602 (1993).
32. Mo, Y. et al. In situ iridium L_{III}-edge X-ray absorption and surface enhanced Raman spectroscopy of electrodeposited iridium oxide films in aqueous electrolytes. *J. Phys. Chem. B* **106**, 3681–3686 (2002).
33. Minguzzi, A. et al. Easy accommodation of different oxidation states of iridium oxide nanoparticles with different hydration degree as water oxidation electrocatalysts. *ACS Cat.* **5**, 5104–5115 (2015).
34. Pfeifer, V. et al. Reactive oxygen species in iridium-based OER catalysts. *Chem. Sci.* **7**, 6791–6795 (2016).

35. Pourbaix, M. J. N. et al. Electrochemical properties of the platinum metals. *Plat.Met. Rev.* **3**, 47–53 (1959).
36. Oh, H. S. et al. Oxide-supported Ir nanodendrites with high activity and durability for the oxygen evolution reaction in acid PEM water electrolyzers. *Chem. Sci.* **6**, 3321–3328 (2015).
37. Birss, V. et al. Electron microscopy study of formation of thick oxide films on Ir and Ru electrodes. *J. Electrochem. Soc.* **131**, 1502–1510 (1984).
38. Augustynski, J. et al. ESCA study of the state of iridium and oxygen in electrochemically and thermally formed iridium oxide films. *J. Electroanal. Chem. Interf. Electrochem.* **160**, 233–248 (1984).
39. Opalka, D. et al. Ab Initio Thermodynamics Insight into the Structural Evolution of Working IrO₂ Catalysts in Proton-Exchange Membrane Electrolyzers. *ACS Cat.* **9**, 4944–4950 (2019).
40. Abbott, D. F. et al. Iridium oxide for the oxygen evolution reaction: correlation between particle size, morphology, and the surface hydroxo layer from operando XAS. *Chem. Mat.* **28**, 6591–6604 (2016).
41. Weber, D. et al. Trivalent iridium oxides: layered triangular lattice iridate K_{0.75}Na_{0.25}IrO₂ and oxyhydroxide IrOOH. *Chem. Mat.* **29**, 8338–8345 (2017).
42. Pfeifer, V. et al. The electronic structure of iridium oxide electrodes active in water splitting. *Phys. Chem. Chem. Phys.* **18**, 2292–2296 (2016).
43. Kötz, R., Neff, H., & Stucki, S. (1984). Anodic Iridium Oxide Films XPS-Studies of Oxidation State Changes and. *Journal of The Electrochemical Society*, *131*(1), 72–77.
44. Sanchez Casalongue, H. G. et al. In situ observation of surface species on iridium oxide nanoparticles during the oxygen evolution reaction. *Ang. Chem. Int. Ed.* **53**, 7169–7172 (2014).
45. Sachse, R. et al. Assessing optical and electrical properties of highly active catalysts for the electrochemical oxygen evolution reaction via spectroscopic ellipsometry. *ACS Cat.* **10**, 14210–14223 (2020).
46. Ping, Y. et al. The reaction mechanism with free energy barriers at constant potentials for the oxygen evolution reaction at the IrO₂ (110) surface. *JACS* **139**, 149–155 (2017).
47. Velasco-Vélez, J. J. et al. Atmospheric pressure X-ray photoelectron spectroscopy apparatus: Bridging the pressure gap. *Rev. Sci. Instr.* **87**, 053121 (2016).
48. Velasco-Vélez, J. J. et al. The Role of Adsorbed and Subsurface Carbon Species for the Selective Alkyne Hydrogenation Over a Pd-Black Catalyst: An Operando Study of Bulk and Surface. *Top. Cat.* **61**, 2052–2061 (2018).
49. Velasco-Velez, J. J. et al. In-situ XAS investigation of the effect of electrochemical reactions on the structure of graphene in aqueous electrolytes. *J. Electrochem. Soc.*, **160**, C445-C450 (2013).
50. Velasco-Velez, J. J. et al. Polarized X-ray Absorption Spectroscopy Observation of Electronic and Structural Changes of Chemical Vapor Deposition Graphene in Contact with Water. *The Journal of Physical Chemistry C*, *118*(44), 25456–25459 (2014).
51. Tuinstra, F. et al. Raman spectrum of graphite. *J. Chem. Phys.* **53**, 1126–1130 (1970).
52. Reich, S. et al, Carbon nanotubes. *Weinheim: Willey-VCH Verlag* (2004).

53. Wang, Y. et al. Raman spectroscopy of carbon materials: structural basis of observed spectra. *Chem. Matt.* **2**, 557–563 (1990).
54. Ismach, A. et al. Direct Chemical Vapor Deposition of Graphene on Dielectric Surfaces. *Nano Lett.* **10**, 1542–1548 (2010).
55. Knop-Gericke, A. et al. In situ X-ray photoelectron spectroscopy of electrochemically active solid-gas and solid-liquid interfaces. *J. Elec. Spec. Rel. Phenom.* **221**, 10–17 (2017).
56. Klyushin, A. et al. Catalyst electronic surface structure under gas and liquid environments. In *Encyclopedia of Interfacial Chemistry*, Elsevier, 615–631 (2018).
57. Giannozzi, P. et al. QUANTUM ESPRESSO: a modular and open-source software project for quantum simulations of materials. *J. Phys.: Condens. Matter* **21**, 395502 (2009).
58. Dal Corso, A. Pseudopotentials periodic table: From H to Pu. *Comput. Mater. Sci.* **95**, 337–350 (2014).
59. Marzari, N. et al. Thermal contraction and disordering of the Al (110) surface. *Phys. Rev. Lett.* **82**, 3296–3299 (1999).
60. Oganov, A.R. et al. Crystal structure prediction using ab initio evolutionary techniques: Principles and applications. *J. Chem. Phys.* **124**, 244704 (2006).
61. Jain, A. et al. Commentary: The materials project: A materials genome approach to accelerating materials innovation. *APL Mater.* **1**, 011002 (2013)
62. Shirley, E. L. Ti 1 s pre-edge features in rutile: a Bethe-Salpeter calculation *J. Electron Spectrosc. Relat. Phenom.* **136**, 77–83 (2004).
63. J. Vinson, J. et al. Bethe-Salpeter equation calculations of core excitation spectra. *Phys. Rev. B* **83**, 115106 (2011).
64. Krause, M. O. et al. Natural widths of atomic K and L levels, K α X-ray lines and several KLL Auger lines. *J. Phys. Chem. Ref. Data* **8**, 329–338 (1979).
65. E. Pehlke, E. et al. Evidence for site-sensitive screening of core holes at the Si and Ge (001) surface. *Phys. Rev. Lett.* **71**, 2338–2341 (1993).
66. Hopfield, J. J. Infrared divergences, X-ray edges, and all that. *Comm. Sol. Sta. Phys.* **2**, 40–49 (1969).
67. Murugappan, K. et al. Operando NAP-XPS unveils differences in MoO₃ and Mo₂C during hydrodeoxygenation. *Nat. Cat.* **1**, 960–967 (2018).
68. O. Bunău and M. Calandra *Phys. Rev. B* **87**, 205105 (2013).
69. J. L Campbell and T. Papp, *Atomic Data and Nuclear Data Tables* **77**, 1–56 (2001).

Figures

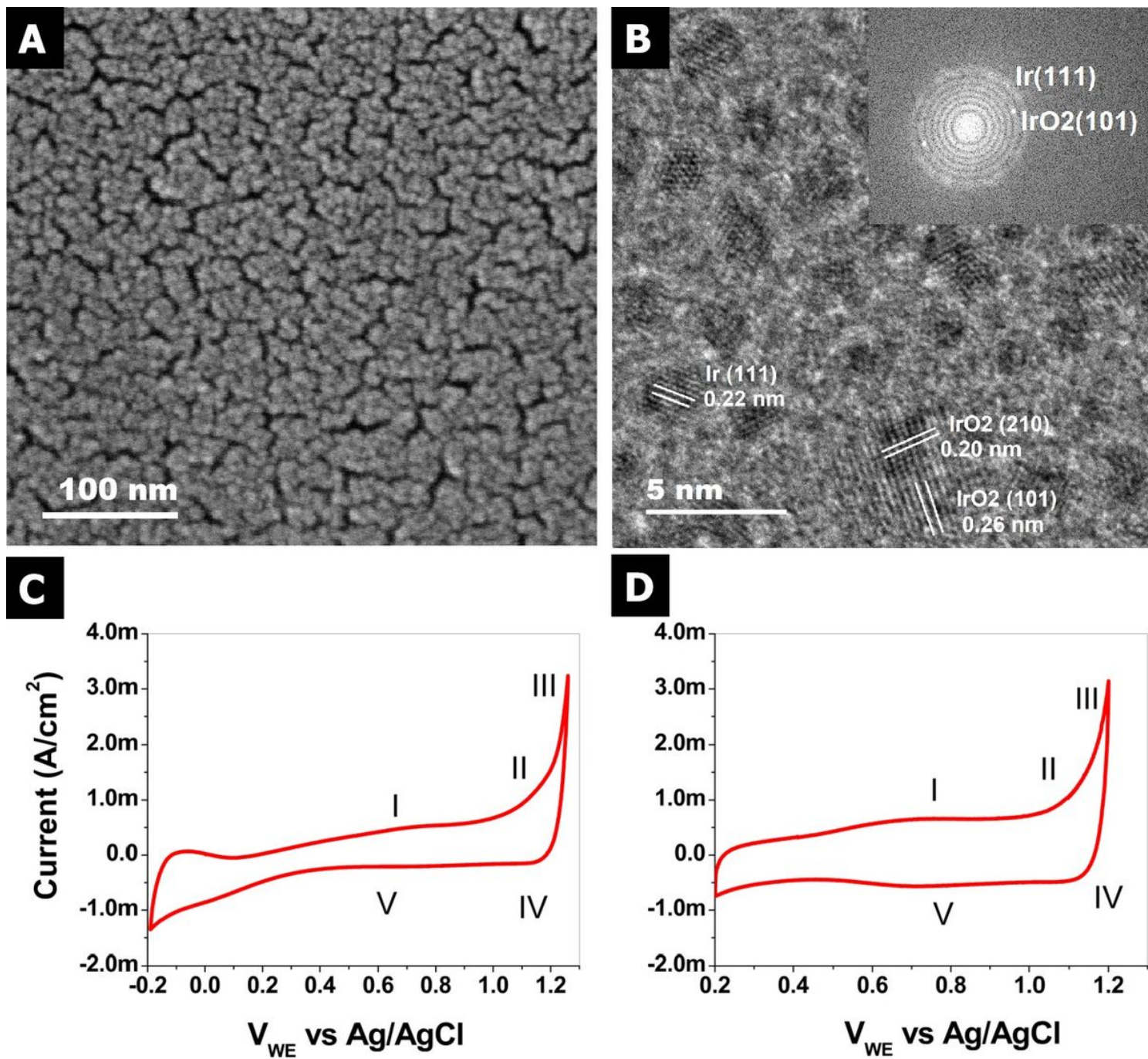


Figure 1

A SEM image of the sputtered thin-film IrO_x electrode. B TEM characterization of the sputtered IrO_x NPs onto the freestanding bi-layer graphene obtained by CVD. CVs of the C thin-film IrO_x electrode and D IrO_x NPs in 100 mM H₂SO₄ with Pt counter and Ag/AgCl reference electrodes, respectively.

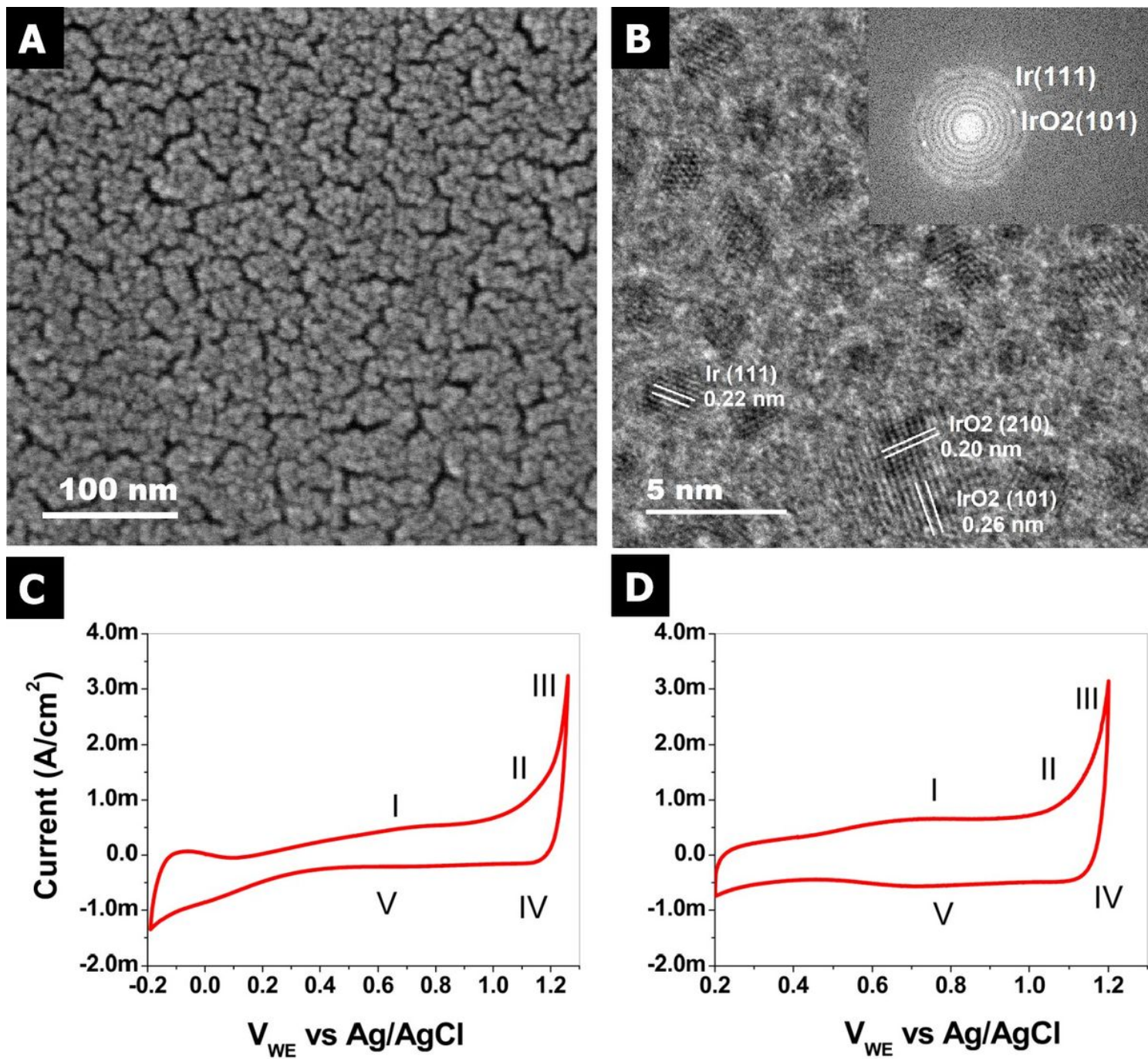


Figure 1

A SEM image of the sputtered thin-film IrO_x electrode. B TEM characterization of the sputtered IrO_x NPs onto the freestanding bi-layer graphene obtained by CVD. CVs of the C thin-film IrO_x electrode and D IrO_x NPs in 100 mM H₂SO₄ with Pt counter and Ag/AgCl reference electrodes, respectively.

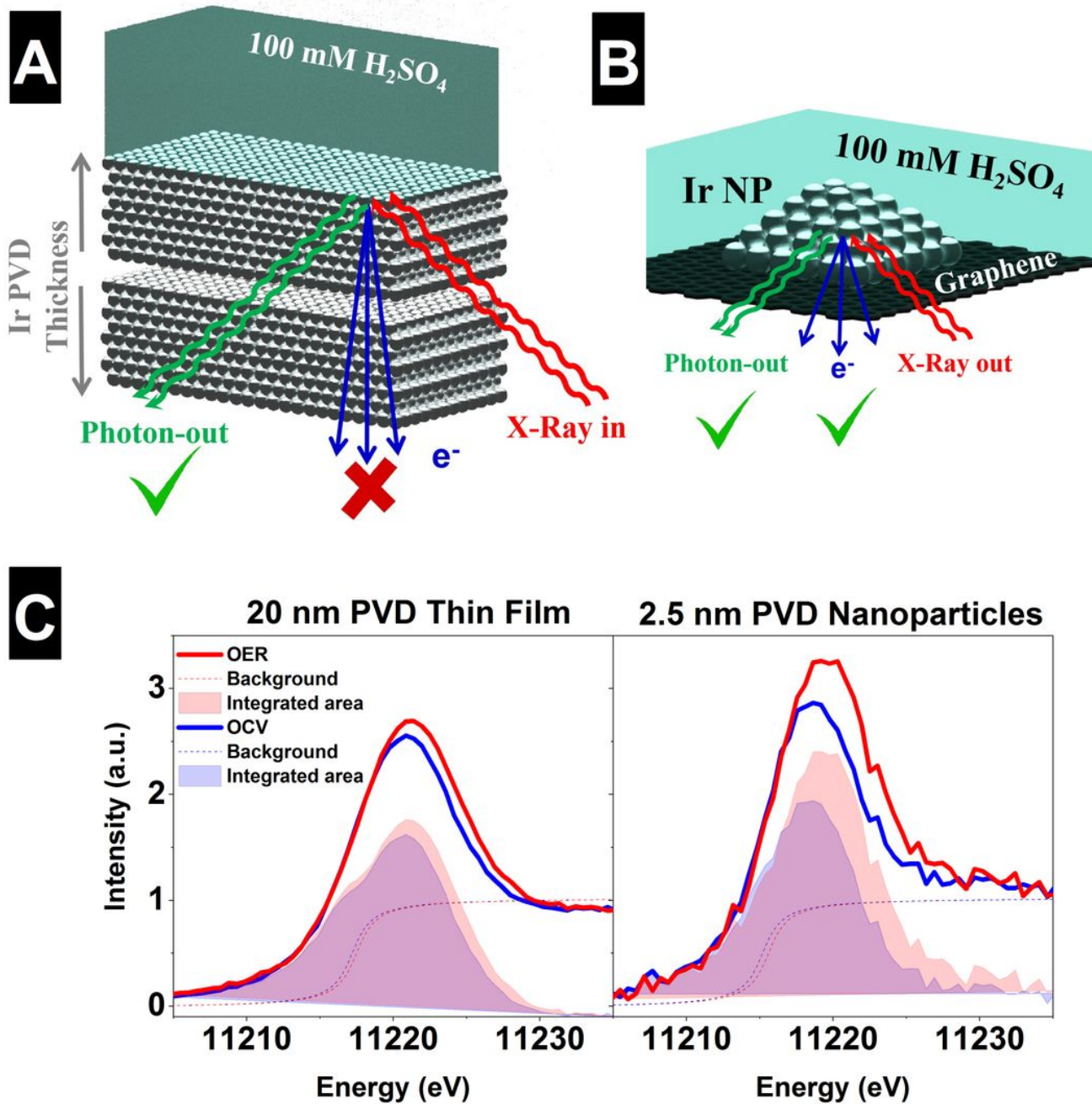


Figure 2

Schematic detection scheme using A a thin-film IrO_x electrode or B free standing CVD bi-layer graphene electrode decorated with IrO_x NPs. Spectra comparison at different potential for the C thin-film IrO_x electrode (20 nm) and free-standing CVD bi-layer graphene electrode decorated with IrO_x 2.5 nm NPs.

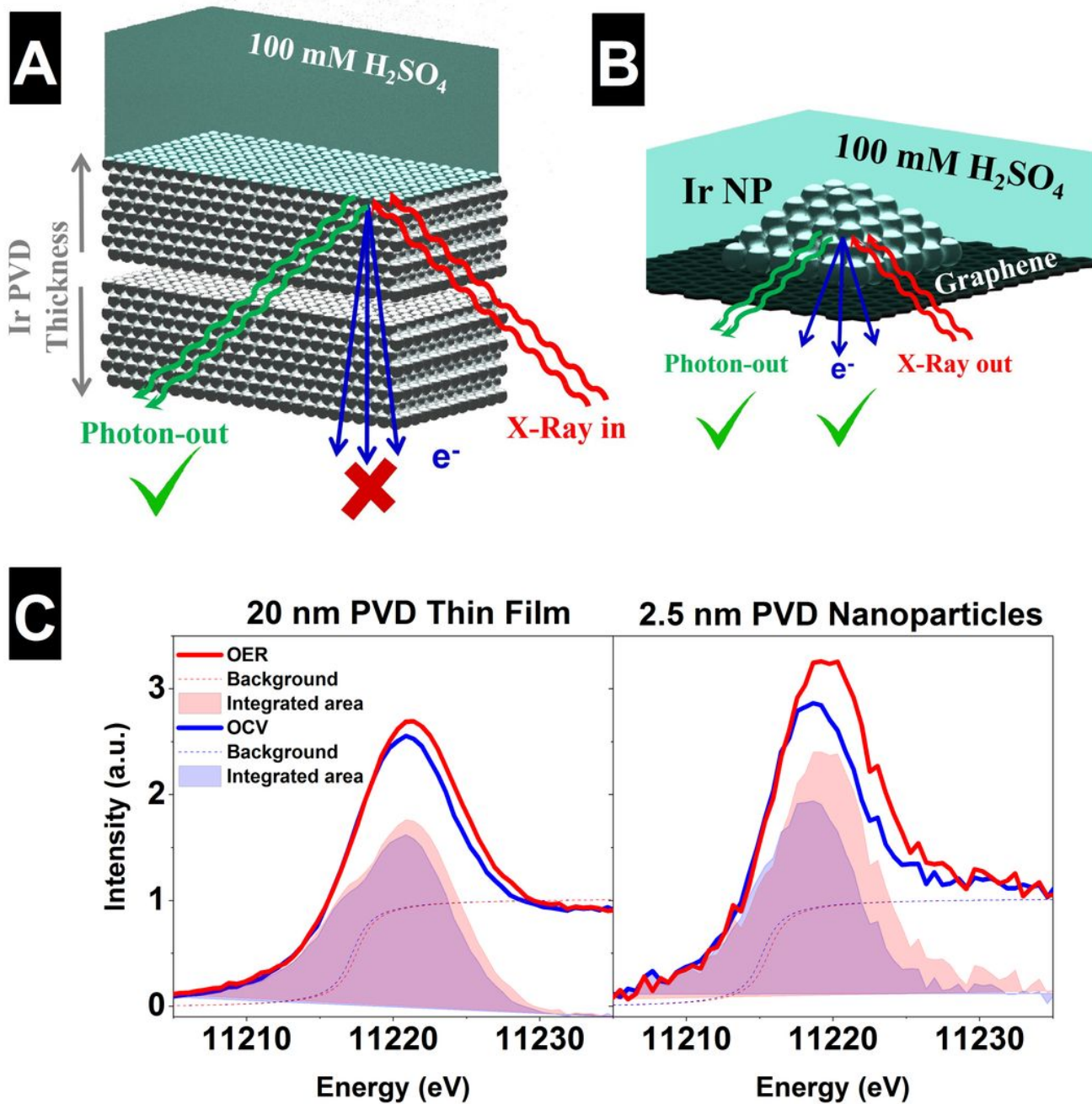


Figure 2

Schematic detection scheme using A a thin-film IrO_x electrode or B free standing CVD bi-layer graphene electrode decorated with IrO_x NPs. Spectra comparison at different potential for the C thin-film IrO_x electrode (20 nm) and free-standing CVD bi-layer graphene electrode decorated with IrO_x 2.5 nm NPs.

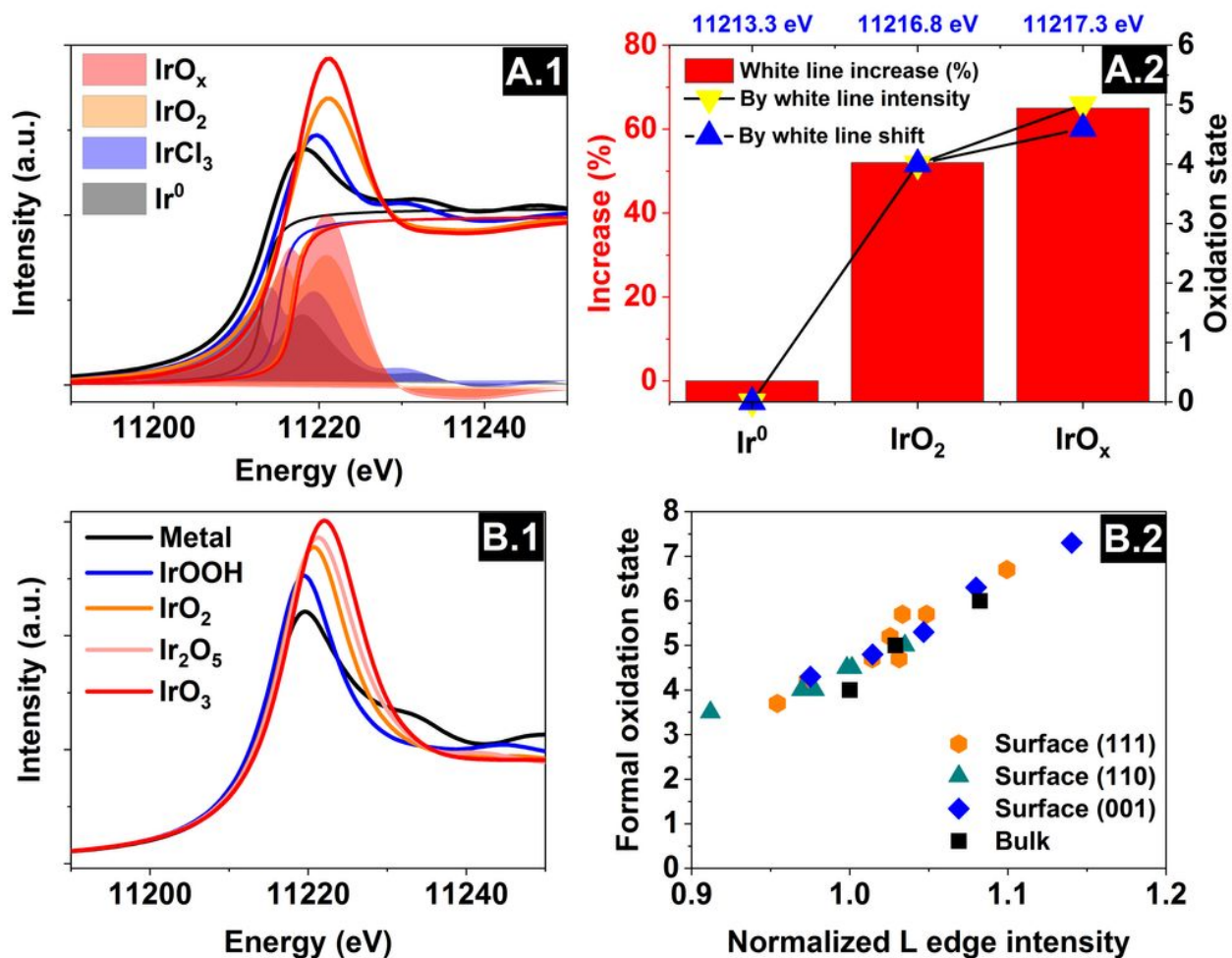


Figure 3

A1 Ir L3 spectra of different reference samples including the background subtraction and remaining signal related to the sum-rule of the Ir 5d electron-holes. A2 Integrated area enhancement referred to IrCl_3 and oxidation state and the estimated oxidation state by white line increase and shift. Calculated B1 Ir L3-edge spectrum of the surface and bulk of an iridium oxides and B2 correlation between computed L3-edge maximum intensity and formal oxidation state.

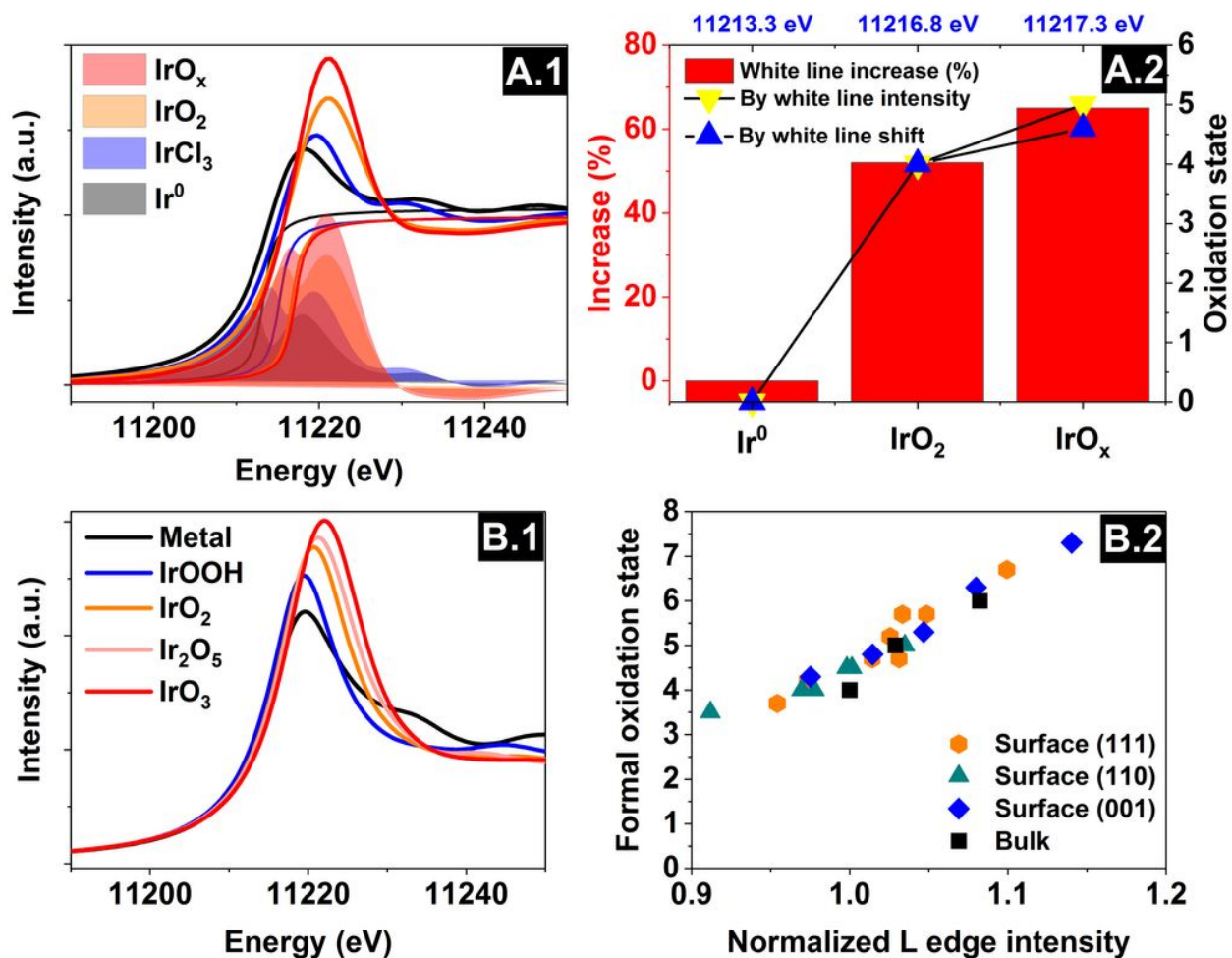


Figure 3

A1 Ir L3 spectra of different reference samples including the background subtraction and remaining signal related to the sum-rule of the Ir 5d electron-holes. A2 Integrated area enhancement referred to IrCl₃ and oxidation state and the estimated oxidation state by white line increase and shift. Calculated B1 Ir L3-edge spectrum of the surface and bulk of an iridium oxides and B2 correlation between computed L3-edge maximum intensity and formal oxidation state.

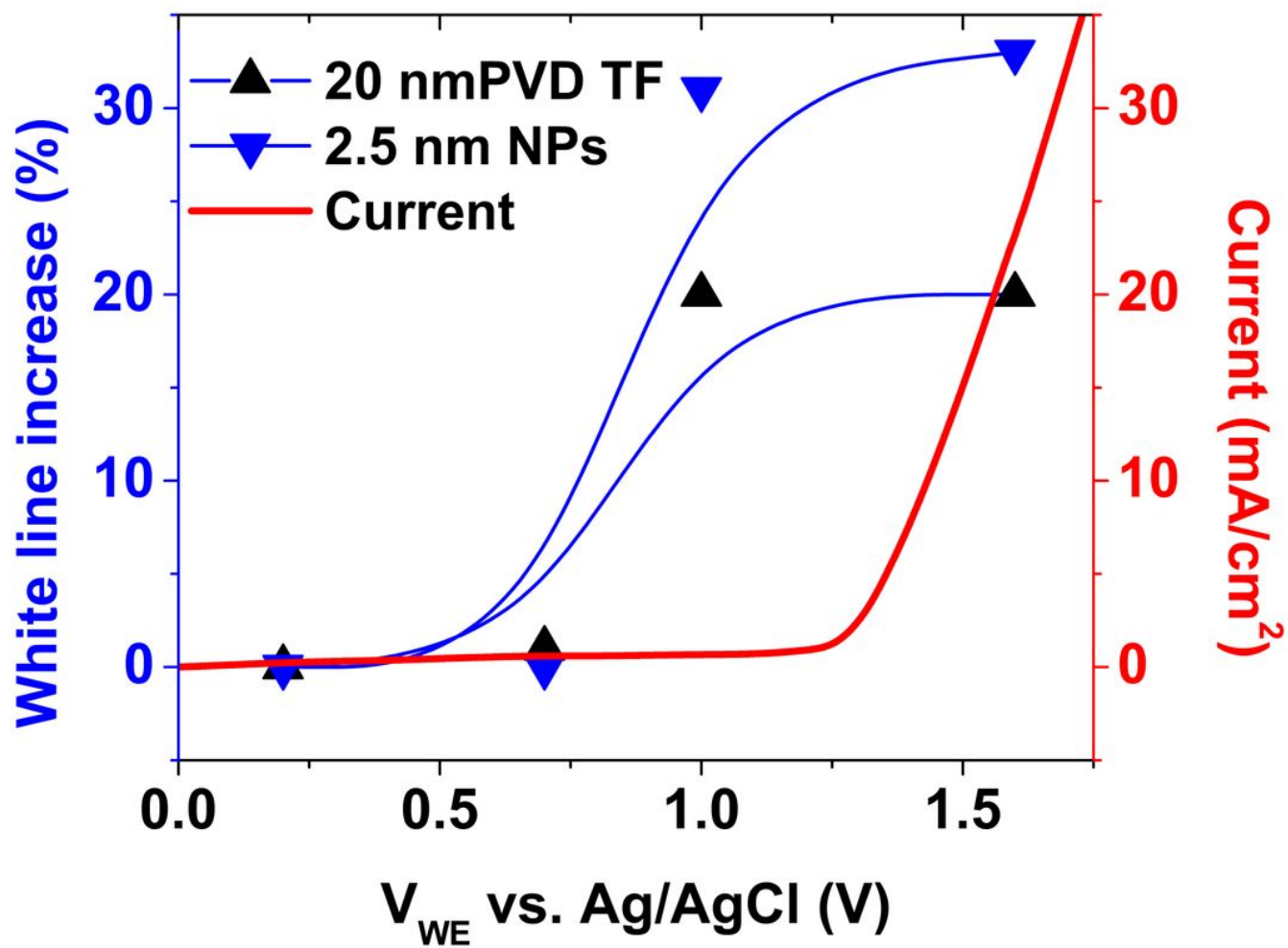


Figure 4

Per cent increase in the hole density and current depending on the working electrode potential recorded during the in situ characterization.

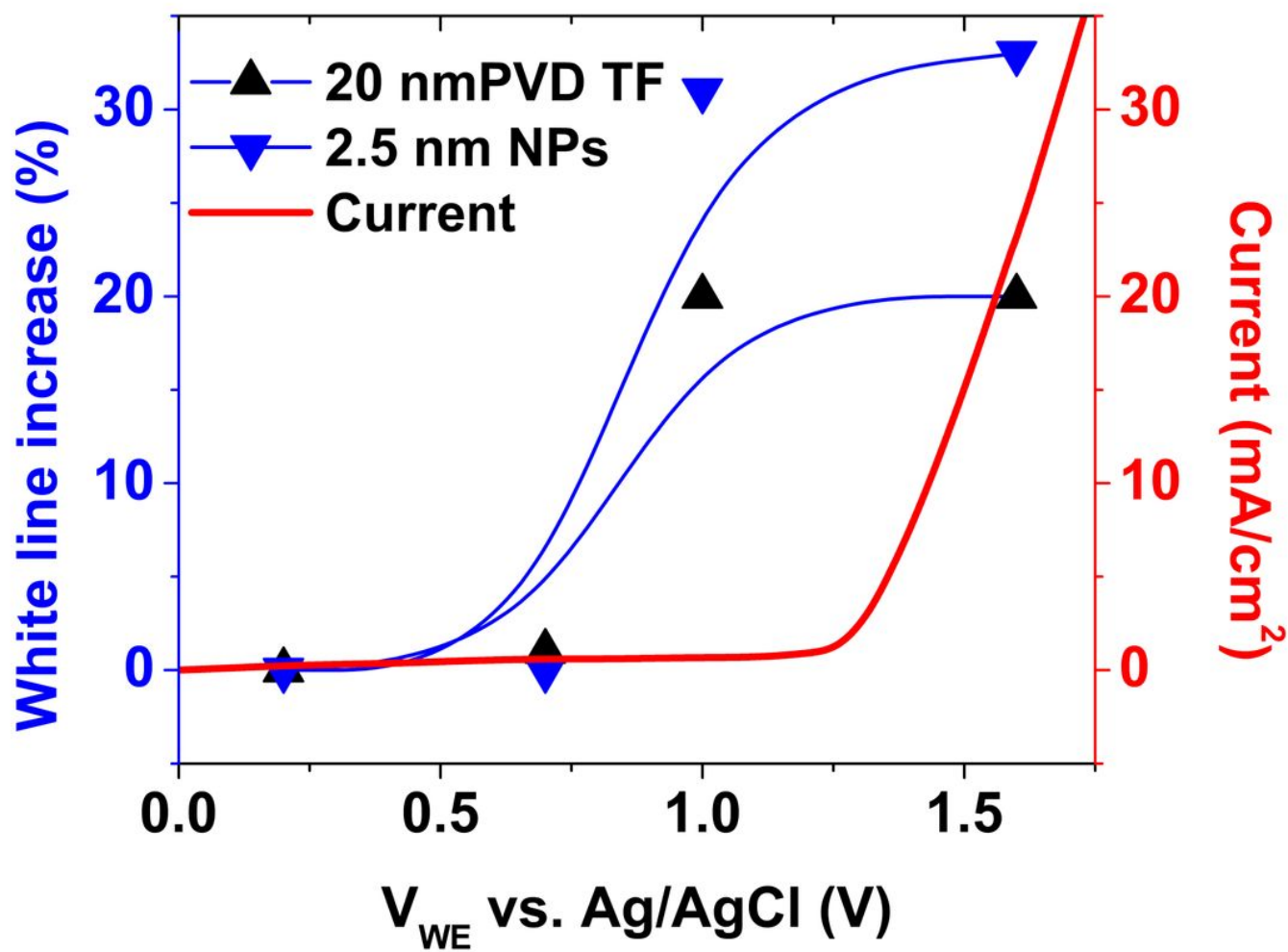


Figure 4

Per cent increase in the hole density and current depending on the working electrode potential recorded during the in situ characterization.

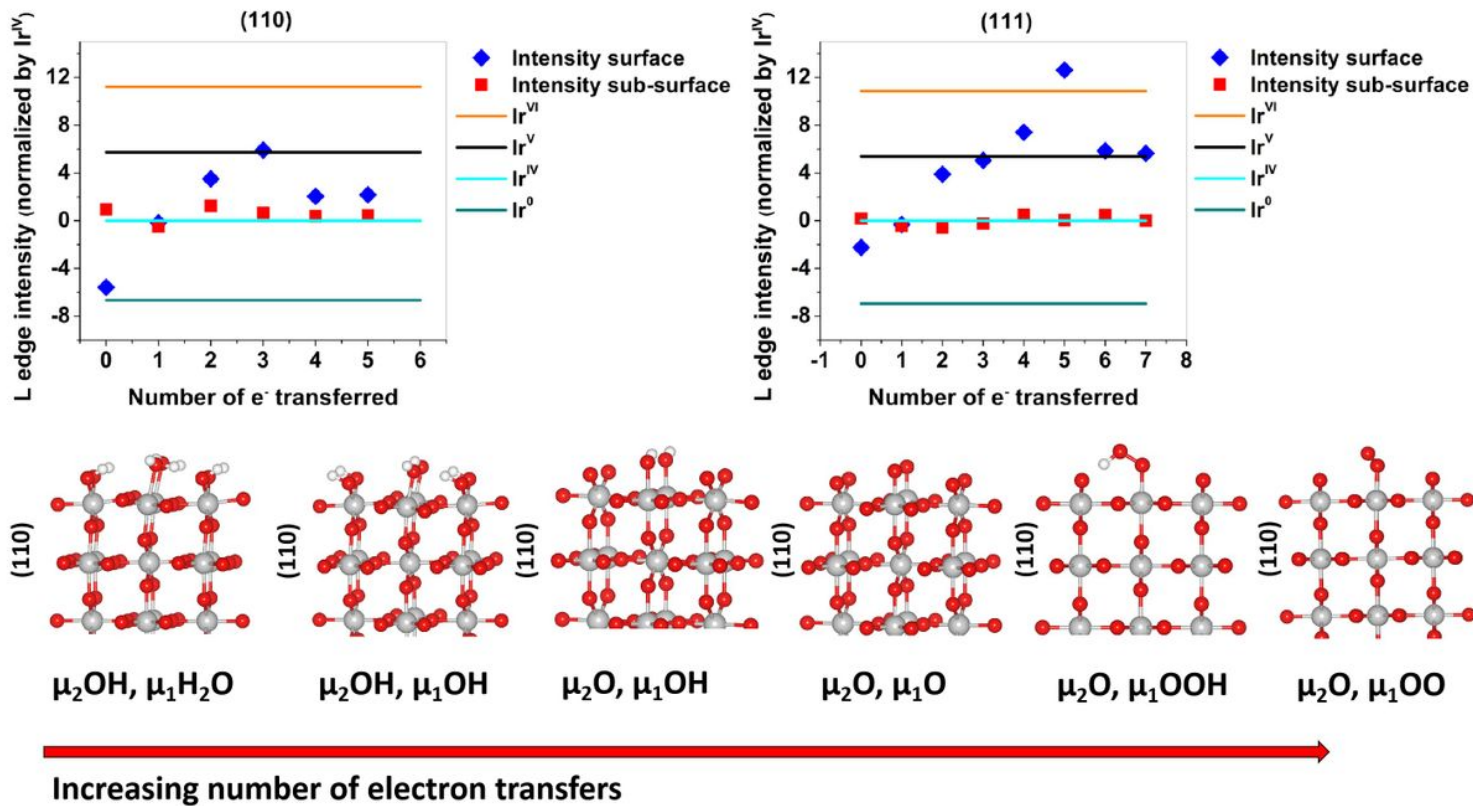


Figure 5

Plots of L3 intensity vs. electron transfers for (110) and (111) surfaces of IrO_2 . On the bottom the different figures are shown for the (110) surfaces. (111) structures are shown in the SI.

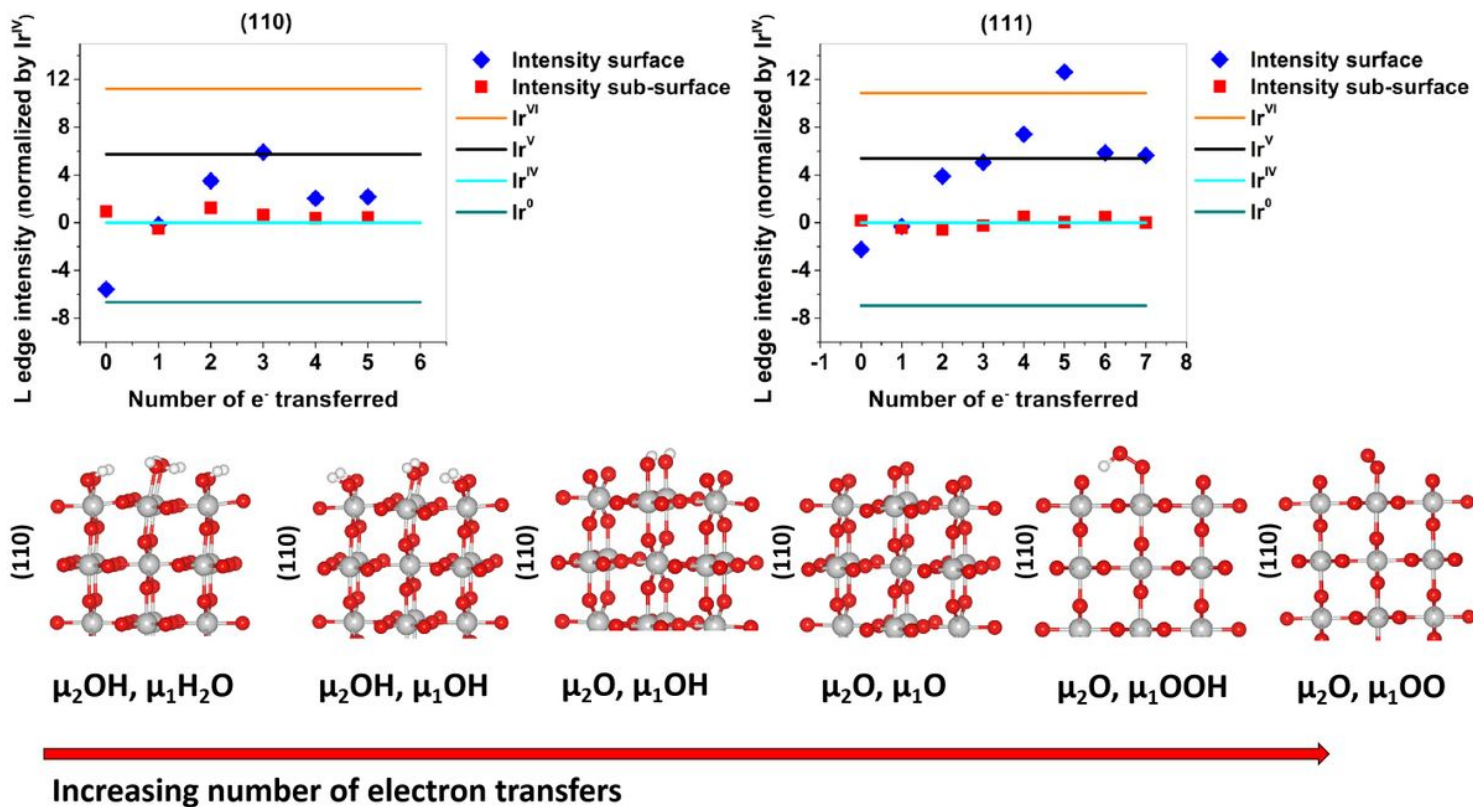


Figure 5

Plots of L3 intensity vs. electron transfers for (110) and (111) surfaces of IrO₂. On the bottom the different figures are shown for the (110) surfaces. (111) structures are shown in the SI.

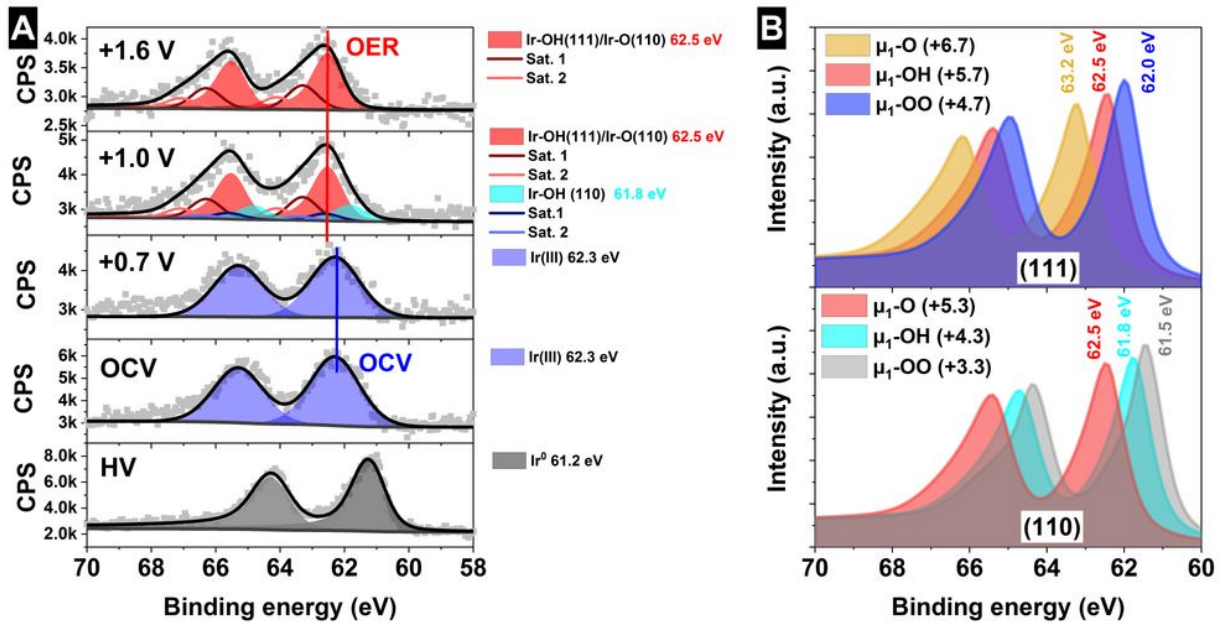


Figure 6

Operando measurements in 100 mM H₂SO₄ of the free standing bi-layer graphene decorated with IrO_x NPs A Ir 4f B simulated Ir 4f spectra of species identified in the Ir L3 edge analysis with the formal oxidation state in brackets.

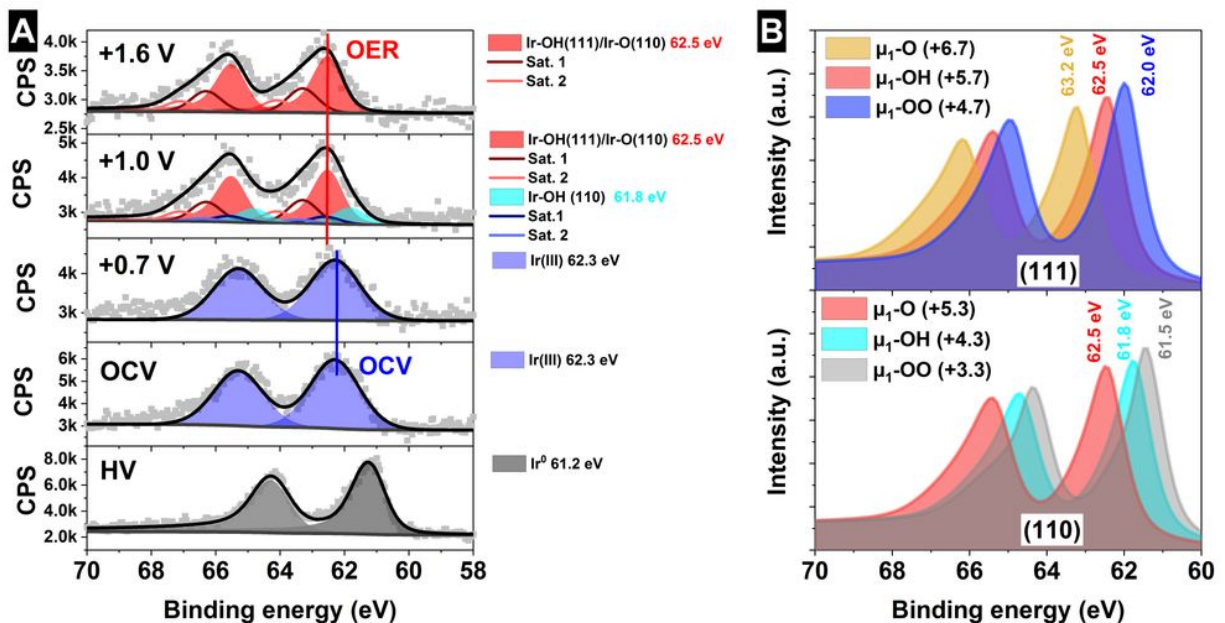


Figure 6

Operando measurements in 100 mM H₂SO₄ of the free standing bi-layer graphene decorated with IrO_x NPs A Ir 4f B simulated Ir 4f spectra of species identified in the Ir L3 edge analysis with the formal oxidation state in brackets.

Supplementary Files

This is a list of supplementary files associated with this preprint. Click to download.

- [VelascoVelezetal.NatureEnergySI2020.docx](#)
- [VelascoVelezetal.NatureEnergySI2020.docx](#)
- [floatimage1.jpeg](#)
- [floatimage1.jpeg](#)